Am J Nucl Med Mol Imaging 2015;5(3):233-245
www.ajnmmi.us /ISSN:2160-8407/ajnmmi0004639

Original Article

The next evolution in radioguided surgery: breast cancer related sentinel node localization using a freehandSPECT-mobile gamma camera combination

Thijs Engelen[1,2], Beatrice MF Winkel[1], Daphne DD Rietbergen[1], Gijs H KleinJan[1,3], Sergi Vidal-Sicart[4], Renato A Valdés Olmos[1,3], Nynke S van den Berg[1,5], Fijs WB van Leeuwen[1,2,5]

[1]Interventional Molecular Imaging Laboratory and Nuclear Medicine section, Department of Radiology, Leiden University Medical Center, Albinusdreef 2, PO Box 9600, 2300 RC, Leiden, The Netherlands; Departments of [2]Head and Neck Surgery and Oncology, [3]Nuclear Medicine, [5]Urology, The Netherlands Cancer Institute - Antoni van Leeuwenhoek Hospital, Plesmanlaan 121, 1066CX, Amsterdam, The Netherlands; [4]Department of Nuclear Medicine, Hospital Clinic-Barcelona, Villarroel 170. 08036 Barcelona, Spain

Received December 9, 2014; Accepted January 9, 2015; Epub February 15, 2015; Published March 1, 2015

Abstract: Accurate pre- and intraoperative identification of the sentinel node (SN) forms the basis of the SN biopsy procedure. Gamma tracing technologies such as a gamma probe (GP), a 2D mobile gamma camera (MGC) or 3D freehandSPECT (FHS) can be used to provide the surgeon with radioguidance to the SN(s). We reasoned that integrated use of these technologies results in the generation of a "hybrid" modality that combines the best that the individual radioguidance technologies have to offer. The sensitivity and resolvability of both 2D-MGC and 3D-FHS-MGC were studied in a phantom setup (at various source-detector depths and using varying injection site-to-SN distances), and in ten breast cancer patients scheduled for SN biopsy. Acquired 3D-FHS-MGC images were overlaid with the position of the phantom/patient. This augmented-reality overview image was then used for navigation to the hotspot/SN in virtual-reality using the GP. Obtained results were compared to conventional gamma camera lymphoscintigrams. Resolution of 3D-FHS-MGC allowed identification of the SNs at a minimum injection site (100 MBq)-to-node (1 MBq; 1%) distance of 20 mm, up to a source-detector depth of 36 mm in 2D-MGC and up to 24 mm in 3D-FHS-MGC. A clinically relevant dose of approximately 1 MBq was clearly detectable up to a depth of 60 mm in 2D-MGC and 48 mm in 3D-FHS-MGC. In all ten patients at least one SN was visualized on the lymphoscintigrams with a total of 12 SNs visualized. 3D-FHS-MGC identified 11 of 12 SNs and allowed navigation to all these visualized SNs; in one patient with two axillary SNs located closely to each other (11 mm), 3D-FHS-MGC was not able to distinguish the two SNs. In conclusion, high sensitivity detection of SNs at an injection site-to-node distance of 20 mm-and-up was possible using 3D-FHS-MGC. In patients, 3D-FHS-MGC showed highly reproducible images as compared to the conventional lymphoscintigrams.

Keywords: Sentinel node, freehandSPECT, nuclear medicine, navigation, radioguided surgery, breast cancer, mobile gamma camera

Introduction

Sentinel node (SN) biopsy is a widely accepted clinical procedure for staging- and grading of cancer types that show lymphatic dissemination, for example breast cancer [1, 2]. Nuclear imaging methods, like planar lymphoscintigraphy and single photon emission computed tomography combined with computed tomography (SPECT-CT), allow accurate preoperative detection of the SNs, and form the basis of this clinical procedure. However, an important part of the effectiveness with which the surgical team can resect the SN(s) depends on their ability to intraoperatively locate the SN(s); the difference in surgical experience may therefore explain the 41-100% range in success rate [3, 4].

Radioguided surgery technologies were shown to aid intraoperative SN identification [5]. Traditionally a gamma-ray detection probe (gamma probe; GP) is used to acoustically trace the SN. More recently the intraoperative use of

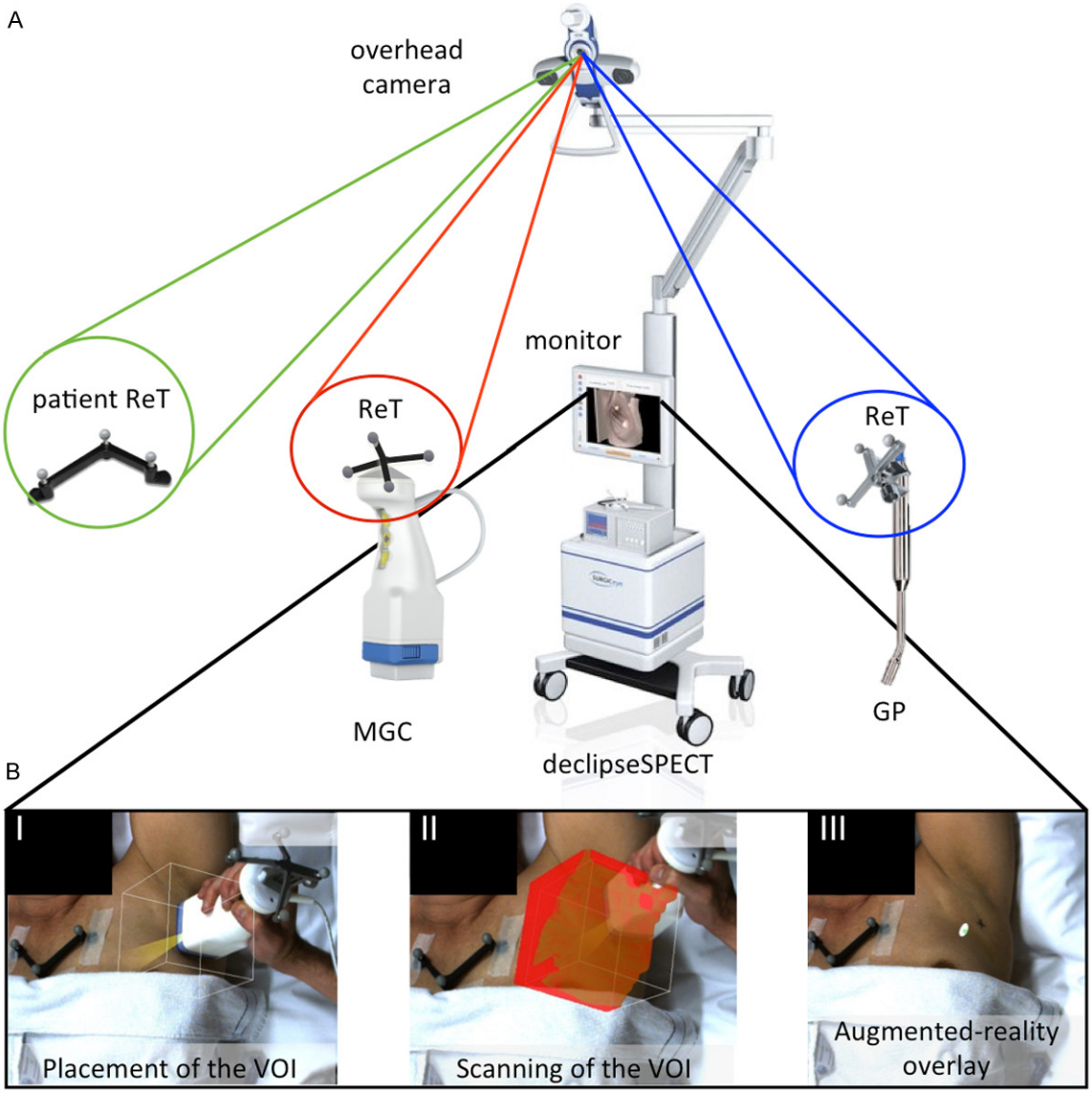

Figure 1. FreehandSPECT acquisition using the declipseSPECT-mobile gamma camera combination. A. Different components of the 3D-freehandSPECT-mobile gamma camera (3D-FHS-MGC) setup. A patient reference tracker (ReT) is placed on the patient. Additional ReTs are placed on the MGC and on the navigation tool (gamma probe (GP)). The position of the patient ReT as well as that of the MGC and the GP are optically tracked by the navigation system. An overhead camera records video-feed. This allows projection of the acquired 3D-FHS-MGC image on the patient thereby generating an augmented-reality image (part B of the figure). B. Generation of a 3D-FHS-MGC scan consists merely of three steps: I) Placement of the volume of interest (VOI) of the MGC over the sentinel node (SN) area; II) Scanning the VOI in three orthogonal directions; and III) Reconstruction of the acquired data results in the generation of a 3D-FHS-MGC augmented-reality image allowing the surgeon to navigate to the SN.

a mobile gamma camera (MGC) was shown to allow 2D SN imaging in the operation theatre thereby improving SN localization and allowing for the confirmation of surgical excision of these nodes [6, 7]. An alternative intraoperative imaging technology, so-called 3D freehand-SPECT (3D-FHS), allows the surgeon to generate an intraoperative 3D SPECT image by scanning an area of interest in three orthogonal directions using a conventional GP [8, 9]. These 3D-FHS-GP images enable the surgeon to visualize the SNs with regard to the current patient position, providing a real-time augmented-reality roadmap in the operation theatre. In addition, in this augmented-reality image, the surgeon can virtually navigate the GP towards the SN(s) [10-14]. Nevertheless, the use of a GP to generate a 3D-FHS image may be associated

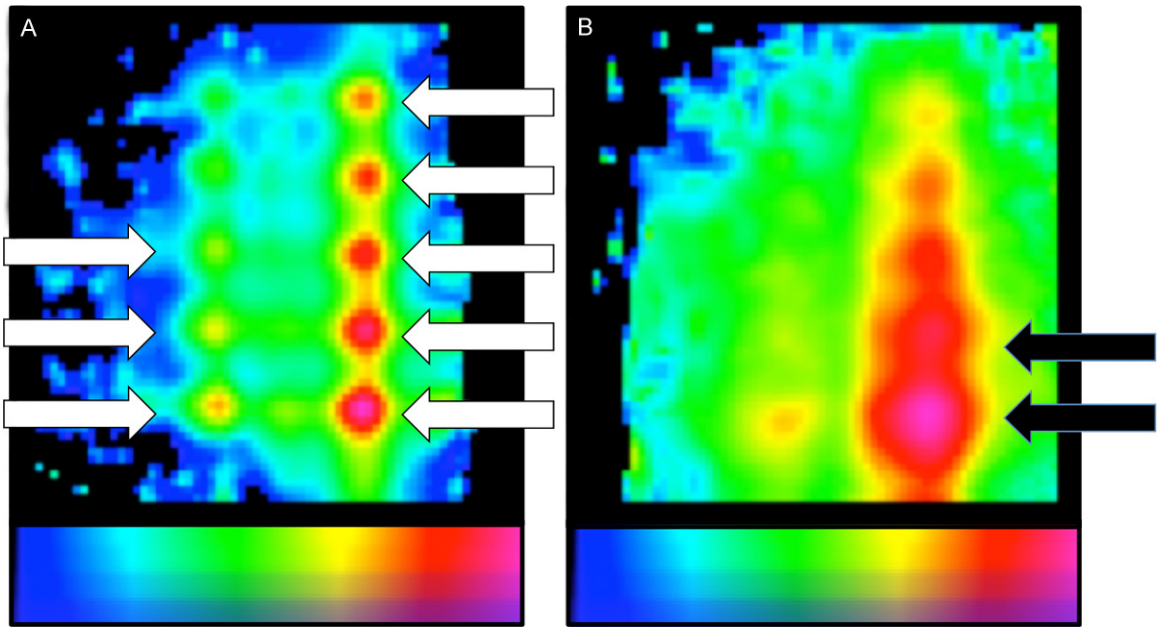

Figure 2. Examples of resolvable and unresolvable nodes. A. Test setup 1 at 4 mm source-detector depth. Eight out of ten hotspots (white arrows) are clearly separable. B. Test setup 1 at 60 mm source-detector depth. No separable hotspots were seen (black arrows). In the scale bars, a blue color represents a low signal intensity and a red color represents a high signal intensity.

with difficulties: The scan time is long due to the small detector surface of the GP and/or the inability to locate SNs in close proximity to the injection site.

Combining the use of the MGC with 3D-FHS resulted in the generation of a "hybrid" modality that transfers the sensitivity benefits of gamma imaging to the 3D-FHS setting. In the current study we present our first results of this new radioguided 3D-FHS-MGC approach. Firstly, the resolvability and sensitivity of the combined system was studied in a phantom setup. Secondly, we evaluated if these findings could be translated to a clinical situation in patients with breast cancer scheduled for SN biopsy.

Patients, materials and methods

FreehandSPECT acquisition

3D-FHS scans were acquired using a navigation system (declipseSPECT, SurgicEye, Munich, Germany) and a MGC (CrystalCam; Crystal Photonics, Berlin, Germany) that was fitted with a low energy high sensitivity Tungsten collimator. The MGC has an energy range of 40-250 KeV, a field of view of 40×40 mm^2 and a resolution of 9.2 mm at a source-detector distance of 35 mm (**Figure 1A**).

Prior to acquisition of the 3D-FHS-MGC scan, a reference tracker (ReT) with fiducial markers was fixed on both the patient (or phantom) and the MGC. Through optical tracking of these fiducials, the declipseSPECT navigation system is able to determine the position of the MGC, and the signal it detects, relative to the patient (or phantom; **Figure 1A**). Before initiation of the acquisition of the 3D-FHS-MGC scan, the marked SN location was placed in the center of the volume of interest (VOI; size 12×12×12 cm) of the MGC. Correct placement of the VOI was confirmed by making an initial 2D overview image with the MGC (hereafter referred to as 2D-MGC).

After verifying correct placement of the VOI (**Figure 1BI**), the declipseSPECT-MGC combination was used to scan the VOI in three orthogonal directions, hereby collecting the radioactive counts present in the VOI (**Figure 1BII**). The collected imaging data was subsequently reconstructed into a 3D-FHS-MGC image by the declipseSPECT system. For image reconstruction a voxel size of 2 mm was used. This voxel size provided the best compromise between image resolution and reconstruction time (the smaller the size of the voxel, the longer the reconstruction time).

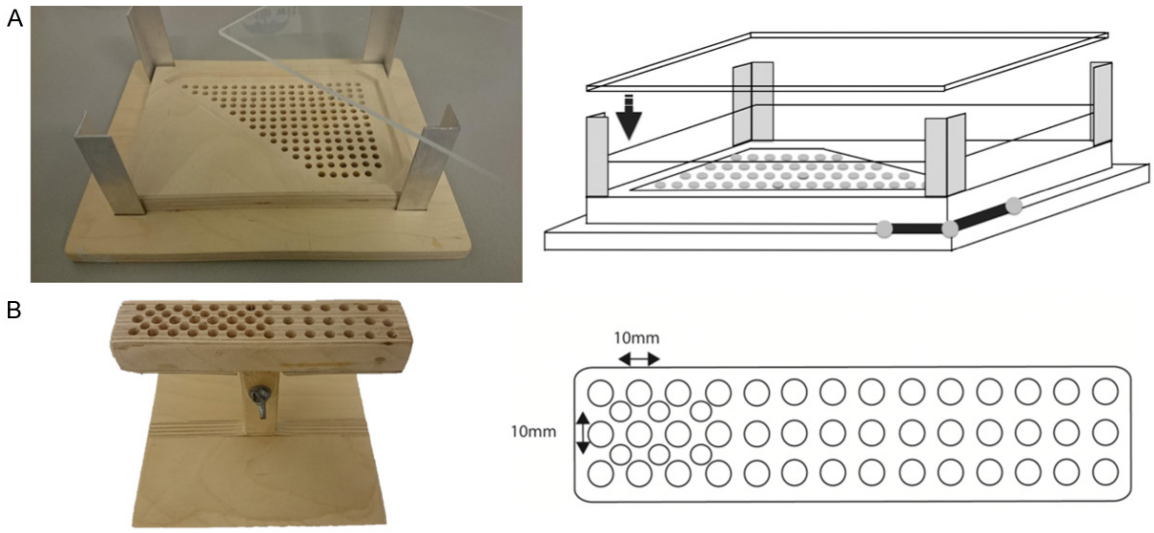

Figure 3. Phantoms. A. Picture and schematic overview of the phantom used for the detection sensitivity and resolution experiments. Diameter of the holes is 5 mm with a hole-hole space of 10 mm. Dimensions of the phantom: 250×170 mm. On the bottom right the reference tracker is drawn. B. Picture and schematic overview of the phantom used for the clustered node experiment. Diameter of the holes is 5 mm with a hole-hole spacing 7 mm. Dimensions of the phantom: 150×40 mm.

The final 3D-FHS-MGC image was then fused with the real-time video feed (2D) generated by the video camera of the navigation system, to allow an augmented-reality view of the area of interest (**Figure 1BIII**). Subsequently a GP (Europrobe 3; Eurorad S.A., Eckbolsheim, France), also containing a ReT with fiducials, was used to navigate towards the SN/hotspot in virtual-reality. The acoustic read-out of the GP was used to verify the accuracy of navigation.

Acquired 2D-MGC and 3D-FHS-MGC images were compared to conventional planar lymphoscintigrams (hereafter referred to as 2D-flatbed; GCA-7100A flatbed gamma camera with a low energy general purpose collimator (Toshiba, Tokyo, Japan)).

In 2D-flatbed and 2D-MGC images a SN/hotspot was considered resolvable when it was clearly separable from the injection site or nearby hotspot (examples of resolvable and unresolvable hotspots are shown in **Figure 2**). In 3D-FHS-MGC the SN/hotspot was considered resolvable when it was depicted as a separate hotspot from the injection site or nearby hotspot, and could be selected for navigation purposes.

Phantom studies

Phantom: To determine the detection sensitivity of the declipseSPECT-MGC combination, a wooden phantom (made out of birch plywood) was used (**Figure 3A**). On this phantom 4 mm plates of Plexiglas Perspex, with a density comparable to that of human muscle and fat tissue [15], could be stacked to vary the source-detector distance and as such to evaluate the in-depth detection efficacy of the declipseSPECT-MGC combination.

A separate birch plywood phantom was used to determine the sensitivity and resolvability of 3D-FHS-MGC in detecting clustered nodes (**Figure 3B**).

Detection sensitivity experiment: Ten ^{99m}Tc-based sources were generated by diluting 10 MBq ^{99m}Tc-pertechnetate with 0.9% NaCl in nine steps down to 19.5 KBq (200 µL per source; dilution range 1:1 to 1:512). Sources were loaded into the phantom in three setups: 1) All together in two rows of decreasing activity (**Figure 4A**); 2) Only the highest dilutions in a single row (1:32-1:512; **Figure 4B**); and 3) The 1:32-1:512 dilutions spaced widely (**Figure 4C**).

2D-flatbed images were obtained of all setups at 12, 32, and 60 mm source-detector depth (image acquisition time: five min). Thereafter 2D-MGC images were generated to determine which sources could be resolved at the various source-detector depths (0-60 mm in steps of 4 mm) (image acquisition time: < 10 sec). Next, 3D-FHS-MGC scans were generated at various

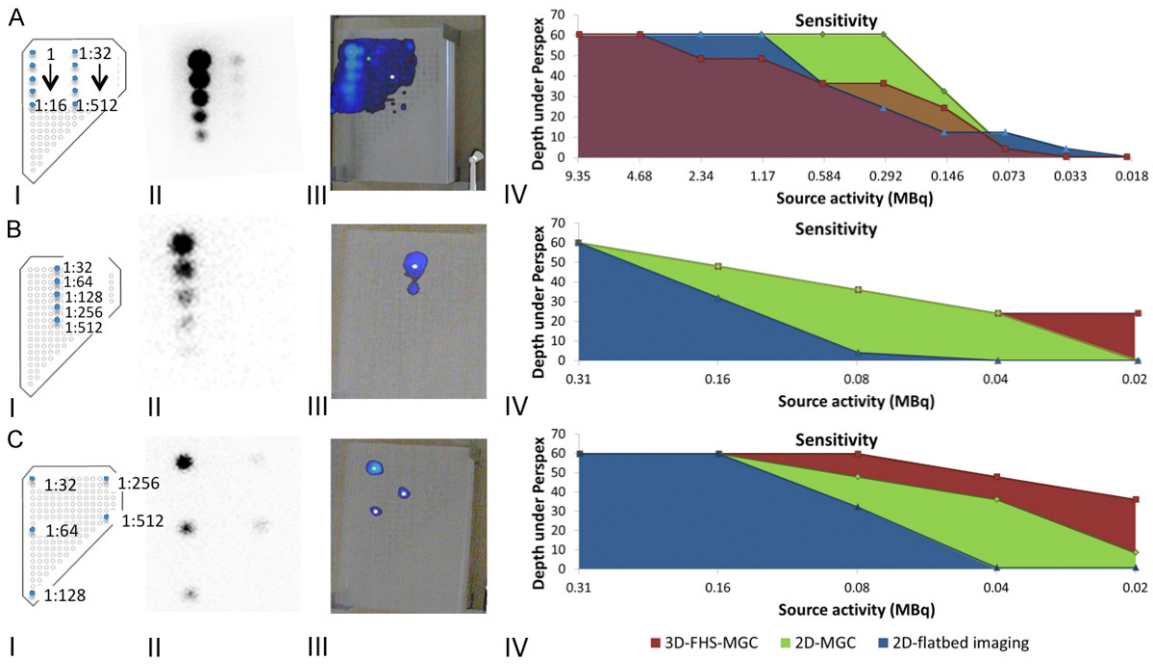

Figure 4. Sensitivity of the 3D-freehandSPECT-mobile gamma camera combination compared to 2D-mobile gamma camera and conventional 2D-flatbed imaging. A. Schematic representation of test setup 1 with all dilutions placed within the VOI. B. Schematic representation of test setup 2 in which only the five highest dilutions were placed in the VOI. C. Schematic representation of test setup 3 in which the five highest dilutions were placed at a respective distance from each other. For all the setups shown: I) Schematic overview of the setup; II) Conventional 2D-flatbed imaging of the various setups at a source-detector depth of 60 mm (acquisition time: five min); III) Corresponding 3D-freehandSPECT-mobile gamma camera (3D-FHS-MGC) image at 60 mm Perspex depth; and IV) Resulting sensitivity graphs. The green line represents 2D-MGC imaging. 2D-flatbed imaging is represented by the blue line and 3D-FHS-MGC by the red line. *Note to setup 3: To make sure all sources fitted inside the VOI during 3D-FHS-MGC scan acquisition the 1:128 source had to be moved so that it was in the centre of the other four sources, so the source seen in the middle in CIII is actually the 1:128 source.*

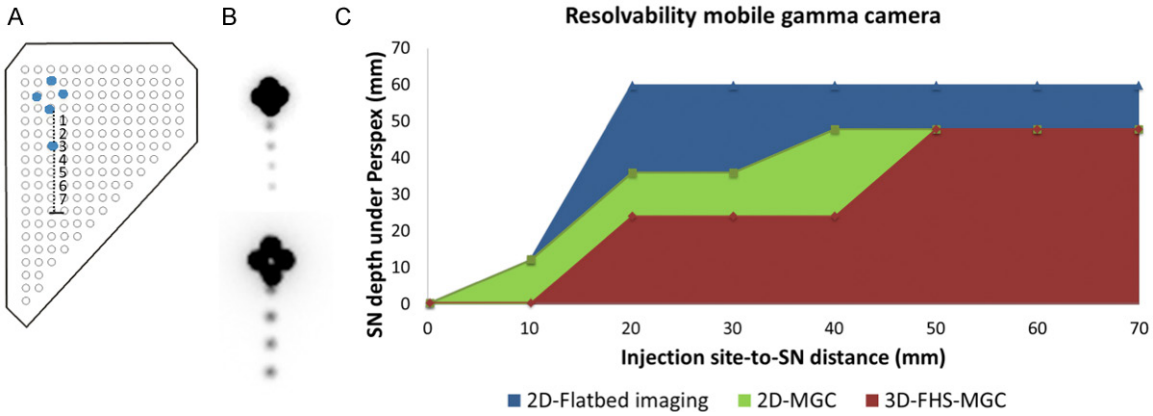

Figure 5. Sentinel node resolvability. A. Schematically representation of the phantom setup. The injection site was simulated using 4×25 MBq ^{99m}Tc-pertechenetate sources placed in a diamond. The sentinel node (SN) was simulated with a 1 MBq ^{99m}Tc-pertechenetate source. Injection site-to-SN distance was varied in steps of 10 mm (range 10-80 mm). B. 2D-flatbed images at a source-detector depth of 60 mm (acquisition time: five min). SNs were placed at 20, 40, 60 and 80 mm injection-site to SN distance at 60 mm depth (upper panel) and 10, 30, 50 and 70 mm at 12 mm depth (lower panel). C. SN resolvability for SNs at various injection site-to-SN distances and various source-detector depths for 2D-flatbed imaging (blue), 2D-MGC imaging (green), and 3D-FHS-MGC (red).

source-detector depths (0-60 mm in steps of 4 mm). After image reconstruction the image was fused with the real-time video feed of the declipseSPECT navigation system and hotspot

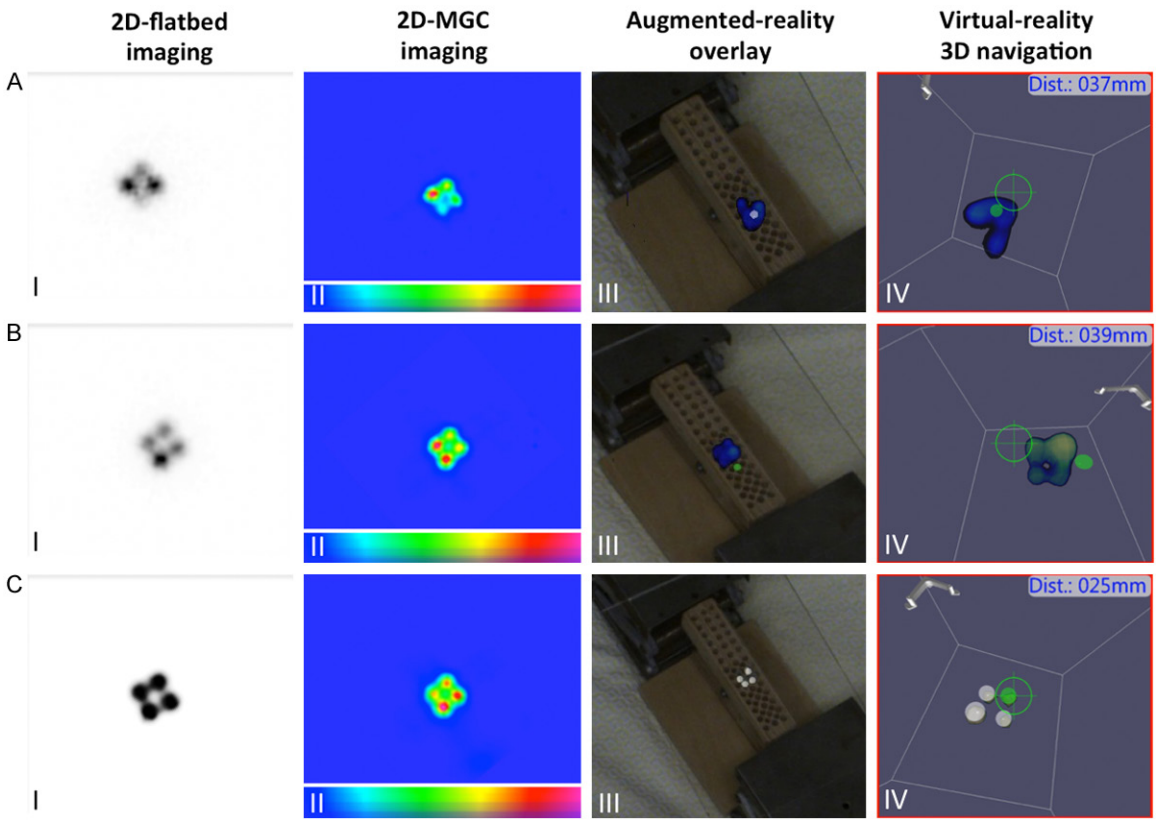

Figure 6. Cluster node resolvability. A. Four ^{99m}Tc-pertechnetate sources of 0.5 MBq placed at 10 mm center-to-center distance from each other. B. Four ^{99m}Tc-pertechnetate sources of 1 MBq placed at 10 mm center-to-center distance from each other. C. Four ^{99m}Tc-pertechnetate sources of 25 MBq placed 10 mm center-to-center distance from each other. The images show: I) 2D-flatbed imaging; II) 2D-mobile gamma camera (MGC) image; III) 3D-freehandSPECT-mobile gamma camera (3D-FHS-MGC) augmented-reality overlay; and IV) virtual-reality navigation to the hotspots. 2D-flatbed, 2D-MGC and 3D-FHS-MGC were only able to separately visualize (and navigate) the 4×25 MBq ^{99m}Tc-pertechentate sources. In the scale bars, a blue color represents a low signal intensity and a red color represents a high signal intensity.

detection sensitivity was evaluated. Acquired images were compared to the sensitivity of 2D-flatbed imaging.

Resolvability experiment simulating near-injection-site sentinel nodes: The effective resolution of 3D-FHS-MGC was determined in an artificial SN setting. For this, an injection site was simulated using four 200 µL sources loaded with 25 MBq ^{99m}Tc-pertechnetate each (total 100 MBq). The SN was simulated by a 1 MBq ^{99m}Tc pertechnetate source (1% of dose at the injection site [16]). The distance between the SN and the injection site was linearly adjusted in steps of 10 mm (range 10-90 mm; source-detector depth 4-60 mm; **Figure 5A**).

2D-flatbed images were generated at 32 and 60 mm source-detector depths (image acquisition time: five min). Thereafter, at various source-detector depths (0-60 mm in steps of 4 mm), 2D-MGC images were generated. Next, 3D-FHS-MGC scans were generated at various source-detector depths (0-60 mm in steps of 4 mm). After image reconstruction the 3D-FHS-MGC image was fused with the real-time video feed and hotspot resolvability was evaluated in augmented- and virtual-reality.

Resolvability experiment clustered nodes: A dedicated phantom experiment was performed to see if clustered nodes could be differentiated from each other. 200 µL Eppendorf tubes were placed in close proximity to each other (10 mm source center-to-center distance) to simulate clustered nodes. Three different setups were generated: 1) 4×0.5 MBq; 2) 4×1 MBq; and 3) 4×25 MBq (**Figure 6**). 2D-flatbed, 2D-MGC and 3D-FHS-MGC images were generated as described for the phantom-resolvability

Table 1. Patient characteristics and preoperative findings

Patients (no.)	10
Age, mean (range)	58 (47-76)
Tumor type	
DCIS	2
Invasive ductal carcinoma	8
Stage	
T*is*	2
T1	4
T2	4
BIRADS	
IV	6
V	1
VI	3
Injected dose ^{99m}Tc-nanocolloid, mean (range)	102 (96-108)
No. SNs/patient, mean (range)	1 (1-2)
Total no. SNs marked by physician	12
Total no. SNs found with 3D-FHS-MGC	11

DCIS = ductal carcinoma in situ; SN = sentinel node; 3D-FHS = Three dimensional freehandSPECT; MGC = mobile gamma camera.

experiment. Acquired 2D-MGC and 3D-FHS-MGC images were compared to 2D-flatbed images.

Patient study

Patients: Between November 2013 and April 2014 ten patients with Tis-T2 breast cancer scheduled for SN biopsy were included after obtaining written informed consent. All patients were clinically node negative as defined by ultrasound and fine needle aspiration cytology. Further patient characteristics are given in **Table 1**. The study protocol was approved by the institutional review board functioning at the Leiden University Medical Center.

Sentinel node resolvability: Patients were injected peri-areolarly with approximately 100 MBq (range 96-108) ^{99m}Tc-nanocolloid (0.2 mL; GE Healthcare, Leiderdorp, the Netherlands). Planar anterior, lateral, and oblique lymphoscintigrams (2D-flatbed images; Toshiba) were obtained 15 min and two hours post-injection with an acquisition time of five min. After image acquisition the nuclear medicine physician marked location of the identified SNs on the skin with indelible ink. Injection site-to-SN distances were measured on the late anterior lymphoscintigram using Osirix medical imaging software (Pixmeo, Geneva, Switzerland).

Thereafter the marked SN location was placed in the center of the VOI and a 2D-MGC image was made. Then a 3D-FHS-MGC scan was generated and fused with the real-time video feed. This allowed hotspot resolvability in augmented-reality and navigation in virtual-reality. Acquired 2D-MGC and 3D-FHS-MGC images were compared to 2D-flatbed images.

Results

Phantom experiments

Detection sensitivity experiment: In three setups (**Figure 4**) a dilution series of ^{99m}Tc sources was imaged via conventional 2D-flatbed imaging, 2D-MGC and the 3D-FHS-MGC imaging. While 2D-MGC image acquisition was real-time with an acquisition time of < 10 sec, 3D-FHS-MGC acquisition took on average 115 sec (range 109-124) with an average reconstruction time of 26 sec (range 17-37) and an average scanned VOI of 69.1% (range 63-73). The resulting sensitivity curves are presented in **Figure 4**.

The detectability of the 1:32-1:512 dilutions was clearly influenced by "overshining" (shine-through) of the sources that contained a high dose ^{99m}Tc-pertechnetate (1:1-1:16 dilutions). Logically, when removing these sources from the setup, the detectability of the sources containing lower activities improved (**Figure 4B**). Best results were obtained when these low activity sources were placed at maximal distance from each other within the VOI (**Figure 4C**).

Overall, 2D-flatbed imaging had the highest detection sensitivity followed by the 2D-MGC imaging and 3D-FHS-MGC (**Figure 4**). The lowest activity that could be detected in 3D-FHS-MGC was 0.08 MBq at a 36 mm source-detector depth. This dose lies well below the clinically reported SN activities of around 1 MBq [16].

Resolvability experiment simulating near-injection-site sentinel nodes: The resolving power of near-injection-site SNs was evaluated for various injection site-to-SN distances and at various depths, and compared to conventional 2D-flatbed images. 3D-FHS-MGC acquisition took on average 121 sec (range 120-124) with

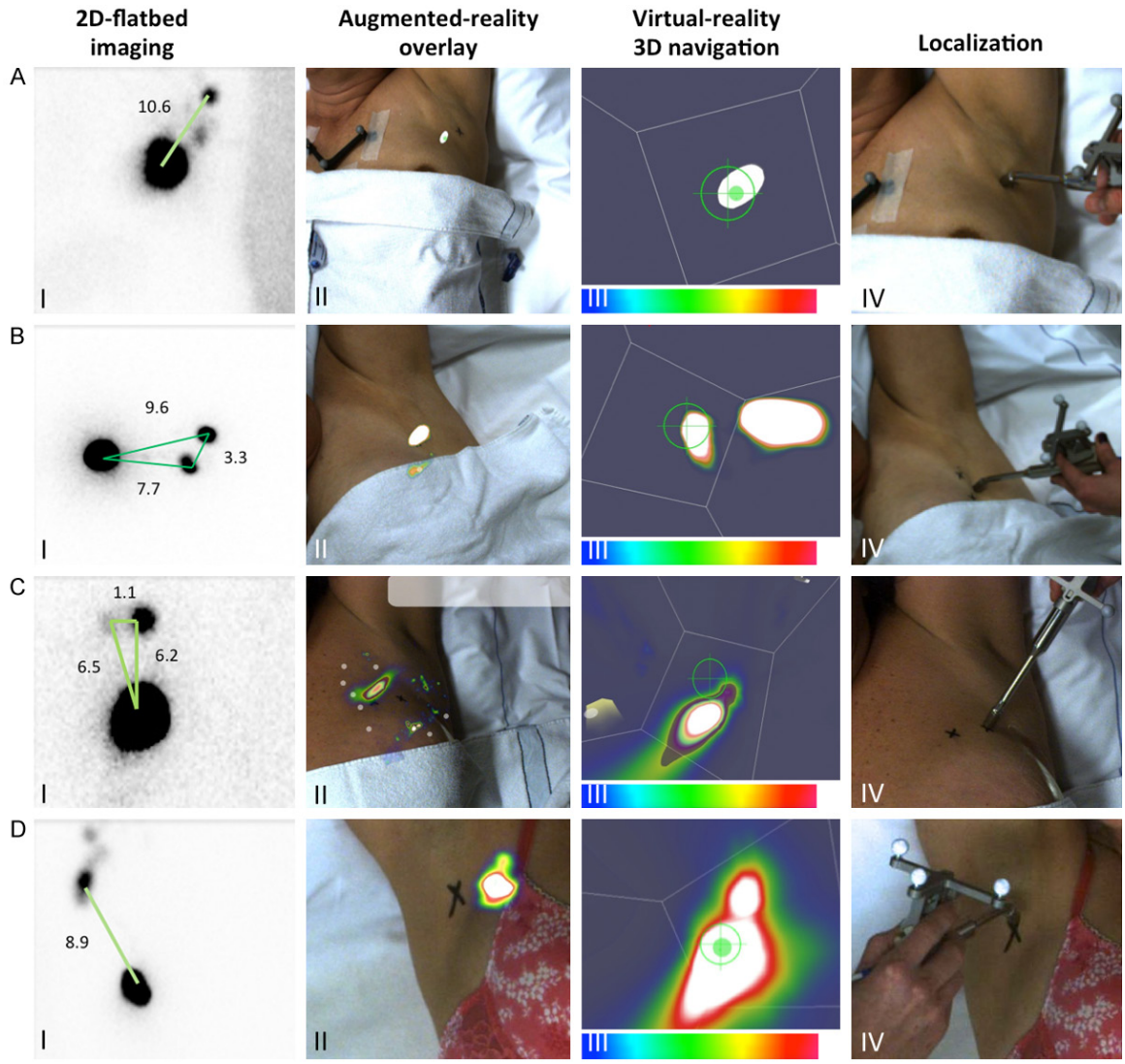

Figure 7. Clinical sentinel node resolvability. A. Patient presenting with a solitary SN in the axilla. I) 2D-flatbed image showing a clear SN. II) 3D-FHS-MGC overlay showing the same SN in the axilla. III) 3D navigation pointing towards the SN in the axilla. IV) Localization of the SN in the axilla. B. Patient with two axillary SNs located 11 mm apart from each other. I) 2D-flatbed imaging showing an intense and a weak hotspot in the axilla. II) 3D-FHS-MGC overlay shows one elongated hotspot. III) 3D navigation shows the same elongated hotspot. IV) Localization points to a spot between the two spots marked by the nuclear medicine physician. C. Patient presenting with an intra-mammary and an axillary SN located at 33mm from each other. I) 2D-flatbed imaging clearly identified two SNs. II) 3D-FHS-MGC overlay also shows two SNs. III) 3D navigation points towards both SNs separately. IV) Successful localization of both SNs. D. Patient with a cluster of 2-4SNs in the axilla. I) 2D-flatbed image showing one hotspot. II) 3D-FHS-MGC shows a hotspot with a protrusion to one side indicating a cluster of SNs. III) 3D navigation shows the protrusion more clearly. IV) Localization points towards the center of the hotspot. In the scale bars, a blue color represents a low signal intensity and a white color represents a high signal intensity.

an average reconstruction time of 32sec (range 16-61) and an average scanned VOI of 83.7% (range 78-91).

Figure 5 shows the obtained resolvability curves for the evaluated modalities. At 60 mm source-detector depth none of the modalities was able to distinguish the SN placed at 10 mm from the injection site, not even 2D-flatbed imaging. At 20 mm injection site-to-SN distance, with 2D-flatbed imaging the SN could already be visualized at 60 mm source-detector depth. 2D-MGC and 3D-FHS-MGC visualized the SN at 20 mm injection site-SN distance at 36 and 24 mm source-detector depth, respectively (**Figure 5**).

Resolvability experiment clustered nodes: To evaluate the ability of the declipseSPECT-MGC combination to resolve SNs in a cluster, a 3D-FHS-MGC scan (average acquisition time 91 sec (range 78-109); average reconstruction time 16 sec (range 9-22) and an average 62.0% scanned VOI (range 50-68)) was acquired of a simulated cluster (four hotspots within 10 mm from each other). The results of this experiment (**Figure 6**) show that in the current setup the 3D-FHS-MGC technology is not able to distinguish hotspots that are located within 10 mm from each other, except when the four sources contained a high amount of radioactivity (25 MBq; **Figure 6C**), and only at a depth of 4 mm. As seen in **Figure 6** the sources of lower activity (4×1 MBq (**Figure 6A**) or 4×0.5 MBq (**Figure 6B**)) are visualized as one single hotspot with 3D-FHS-MGC.

Patient study

In all ten breast cancer patients lymphoscintigraphy identified at least one axillary SN. Preoperative imaging revealed a total of 12 SNs (range 1-2 SNs per patient). The number of SNs visualized was the same on both early and late lymphoscintigrams. The average injection site-to-SN distance was 93 mm (range 38-150), as determined on the late anterior lymphoscintigrams. Two of the ten patients presented with two axillary SNs in which the SN-SN distance was 33 mm and 11 mm, respectively (**Figure 7B** and **7C**). One patient presented with a cluster of 2-4 SNs that could not be separated with lymphoscintigraphy (**Figure 7D**).

2D-MGC imaging took < 10 sec. 3D-FHS-MGC acquisition took on average 112 sec (range 61-156) with an average reconstruction time of 61sec (range 45-99)). On average 61% of the VOI was scanned (range 46-87). In nine out of ten included patients the number of SNs as seen on the planar lymphoscintigrams was equal to the number of SNs seen with 2D-MGC imaging and 3D-FHS-MGC (examples are given in **Figure 7**). This resulted in an 91.7% resolvability for both 2D-MGC and 3D-FHS-MGC imaging (11 out of 12 SNs detected).

In one patient, on the acquired lymphoscintigrams two adjacent axillary SNs (11 mm apart) were seen. One very intense SN and one very faint SN. However, neither 2D-MGC nor the 3D-FHS-MGC could differentiate these two nodes (**Figure 7C**). These findings are in line with the results of the resolvability phantom experiment, where sources closer than 20 mm could not be resolved. In another patient presenting with two SNs located at 33 mm apart from each other on the anterior planar lymphoscintigram, the SNs were clearly separable with 3D-FHS-MGC (**Figure 7B**), which was again in concordance with the phantom results.

Interestingly, in one patient planar lymphoscintigrams indicated a single hotspot consisting of a cluster of 2-4 SNs according to the nuclear medicine physician (**Figure 7D**). 3D-FHS-MGC showed protrusions on one side of the hotspot, indicating an irregular distribution of radioactivity in this region, representative of a cluster of SNs of equal (low) activity, which could not be visualized separately as was also seen in the cluster phantom experiment.

Discussion

In the phantom study we found that the resolvability of the various radioactive sources strongly depended on 1) injection site-to-SN distance; and 2) the source-detector depth. These findings are in concordance with findings of conventional 2D-flatbed imaging. The validity of the 3D-FHS-MGC approach was demonstrated in patients with breast cancer where the technique identified 11 out of 12 SNs, and allowed virtual-reality-based navigation to all visualized SNs.

We found that by using the MGC for 3D-FHS acquisition, instead of a GP, the ease of data acquisition increased while the acquisition time decreased due to the higher sensitivity of the MGC for gamma detection; the detector area of the MGC is approximately 32 times larger than that of the GP used in our study. Moreover, during data acquisition the MGC provides the surgeon with a visual image of the area harbouring radioactivity whereas the GP only provides an acoustic read-out of detected radioactivity.

It was difficult to resolve low activity sources when a high activity source was present within the VOI, or when the SNs were located close to each other in e.g. a cluster. This effect is the result of “overshining”, which is one of the major limitations in radioguided surgery [17]. In the current system setup scaling of the 3D-FHS-MGC image is set to the highest activity source

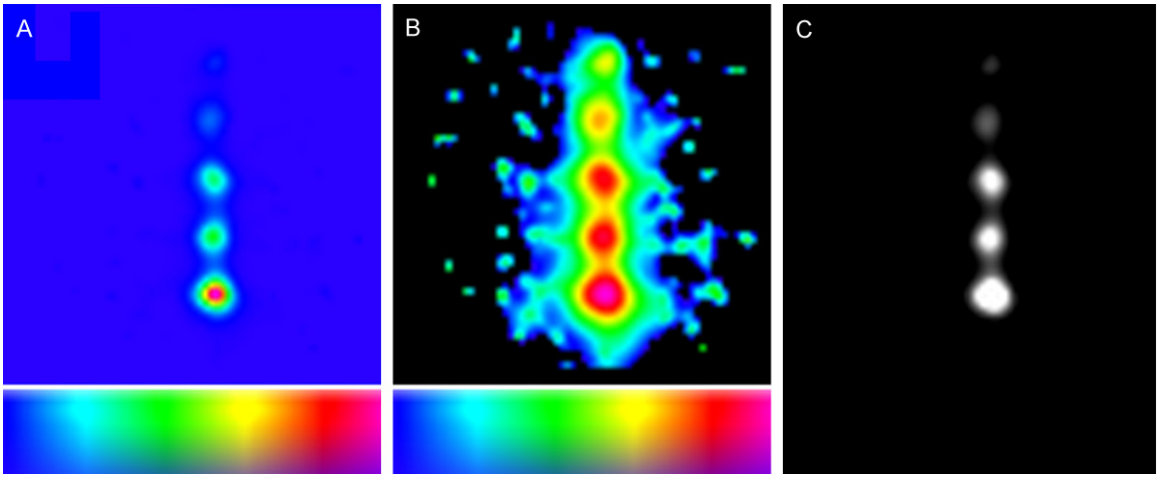

Figure 8. Improved reconstruction algorithms help improve the data that is shown in the 3D-freehandSPECT-mobile gamma camera image. The images show an example of test setup 2 of the sensitivity experiment at a source-detector depth of 24 mm. A. Summation of volume data in z-direction when a linear transfer function is used. This data is currently displayed by the declipseSPECT system after reconstruction of the 3D-freehandSPECT-mobile gamma camera (3D-FHS-MGC) scan. B. Summation of volume data in z-direction when a logarithmic transfer function is used. Clearly in this setting more information is displayed than in *A*. C. A single volume slice from test setup 2. In Osirix medical imaging software (Pixmeo) the logarithmic transfer function is shown with the window leveling set to display all hotspots. In the scale bars, a blue color represents a low signal intensity and a red color represents a high signal intensity.

within the VOI. As a consequence of this scaling, low activity sources within the VOI are lost when high activity sources are present, as was shown in both the phantom and patient studies. With the VOI being set at 12×12×12 cm, in most patients, next to the SN (part of) the injection site was also present within the area that was scanned. By narrowing the VOI, the influence of the activity coming from the injection site may be reduced. An alternative solution for the "overshining" effect could be to remove the counts measured at the injection site from the 3D-FHS-MGC reconstruction, thus by (digitally) blocking the counts from the higher activity source (injection site). Consequently scaling will be performed on the remaining hotspot(s) and these will then become more pronounced. This method has been previously described for an alternative MGC system [7]. Yet, in order to take advantage of this feature, good knowledge on the location where the blocking has to be performed is required.

Improved detectability of hotpots with a higher activity also has its advantages; when low activity containing higher-echelon nodes are located within the same VOI as the SN, only the SN will be resolved in 3D-FHS-MGC. This may be especially beneficial in areas such as the head and neck or groin where often multiple higher-echelon nodes are reported [18]. Preferably technical solutions for "overshining" can be switched on and off at the discretion of the surgeon.

In the current phantom and clinical study, resolvability of clustered SNs and SNs in close proximity to each other was not yet possible. This is most likely the consequence of the spatial resolution of the current camera (9.2 mm at 35 mm source-detector distance). This might be improved by using a higher resolution imaging device [19-23] that can also be made compatible with the declipseSPECT navigation system. It may further ease the implementation of this combined declipseSPECT-MGC approach in the clinical workflow. However, a potential downside would be the fact that an increase in spatial resolution goes hand-in-hand with a reduction in sensitivity of the camera.

It was found that SN visualization within the VOI could be greatly improved by using different 3D-FHS-MGC reconstruction parameters. Unfortunately this resulted in a large increase in reconstruction time. When the generated 3D-FHS-MGC images were imported in the Osirix image viewer (Pixmeo), scaling could be used to increase the visibility (an example is given in **Figure 8**). This indicates further software improvements to the declipseSPECT view-

Table 2. Radioguidance modalities

	Gamma camera	SPECT	Gamma probe	MGC	FHS-MGC*
Readout	Visual, 2D	Visual, 3D	Acoustic signal	Image, 2D	Image, 3D + acoustic*
SN mapping					
preoperative	Y, 2D	Y, 3D	N	Y, 2D	Y, 2D
intraoperative	N	N	N	Y, 3D	Y, 3D
Correlation nuclear image with anatomy of the patient	N	Y, when overlayed with CT	N	N	Y, when overlayd with real-time video feed (augmented-reality)
Potential for navigation	N	Y, when data sets are imported in the declipseSPECT navigation device [14]	N	N	Y*, virtual navigation option included in the technology

*When used in combination with the integrated gamma probe. SPECT = single photon emission computed tomography; CT = computed tomography; MGC = mobile gamma camera; FHS = freehandSPECT; 2D = two dimensional; 3D = three dimensional; SN = sentinel node; Y = yes; N = no.

er may be an easy was to generate progress in this area.

Although this newly evaluated "hybrid" radioguidance technology is not yet able to solve two of the major limitations encountered during radioguided SN biopsy (the identification of near-injection-site SNs and separation of cluster nodes), it does provide rapid and clear visibility of hotspots relative to the anatomic context of the patient (video feed; augmented-reality) and subsequently the possibility to virtually navigate towards these SNs, thereby possibly improving the localization process. This technique also provides integration of five otherwise separately used image-guided surgery technologies, namely: a GP, an MGC, 3D-FHS, augmented-reality display, and virtual navigation (**Table 2**). The "hybrid" radioguidance technology, whereby the strengths of the individual technologies remain preserved, and are complemented by the strengths of the other modalities, not only improves surgical logistics, but also provides perspective for more complex radioguided procedures in the future.

Conclusion

In this translational study, initial phantom evaluation of MGC-based 3D-FHS was followed by its clinical evaluation in patients with breast cancer. The data showed a high degree of concordance in superficial areas (< 60 mm) with conventional 2D-flatbed images. In our view this 3D-FHS-MGC approach may be of value in indications where SNs are generally located within 60 mm from the skin such as head and neck tumors or melanoma.

Acknowledgements

This work was partially supported by a Dutch Cancer Society translational research award (Grant No. PGF 2009-4344) and an NWO-STW-VIDI grant (Grant No. STW-BGT11272). We gratefully acknowledge the entire nuclear medicine division of the LUMC for their contribution.

Disclosure of conflict of interest

None.

Address correspondence to: Nynke S van den Berg, Interventional Molecular Imaging Laboratory, Department of Radiology, C2-S zone, Leiden University Medical Center, Albinusdreef 2, 2300 RC, Leiden, The Netherlands. Tel: +31 (0)71 526 2042; E-mail: N.S.van_den_Berg@lumc.nl

References

[1] Nieweg OE, Tanis PJ and Kroon BB. The definition of a sentinel node. Ann Surg Oncol 2001; 8: 538-541.

[2] Morton DL, Wen DR, Wong JH, Economou JS, Cagle LA, Storm FK, Foshag LJ and Cochran AJ. Technical details of intraoperative lymphatic mapping for early stage melanoma. Arch Surg 1992; 127: 392-399.

[3] Kim T, Giuliano AE and Lyman GH. Lymphatic mapping and sentinel lymph node biopsy in early-stage breast carcinoma: a metaanalysis. Cancer 2006; 106: 4-16.

[4] Schirrmeister H, Kotzerke J, Vogl F, Buck A, Czech N, Koretz K, Helm G, Kreienberg R and Kuhn T. Prospective evaluation of factors influencing success rates of sentinel node biopsy in 814 breast cancer patients. Cancer Biother Radiopharm 2004; 19: 784-790.

[5] Warncke SH, Mattei A, Fuechsel FG, Z'Brun S, Krause T and Studer UE. Detection rate and operating time required for gamma probe-guided sentinel lymph node resection after injection of technetium-99m nanocolloid into the prostate with and without preoperative imaging. Eur Urol 2007; 52: 126-132.

[6] Olcott P, Pratx G, Johnson D, Mittra E, Niederkohr R and Levin CS. Clinical evaluation of a novel intraoperative handheld gamma camera for sentinel lymph node biopsy. Phys Med 2014; 30: 340-345.

[7] Vermeeren L, Valdes Olmos RA, Meinhardt W, Bex A, van der Poel HG, Vogel WV, Sivro F, Hoefnagel CA and Horenblas S. Intraoperative radioguidance with a portable gamma camera: a novel technique for laparoscopic sentinel node localisation in urological malignancies. Eur J Nucl Med Mol Imaging 2009; 36: 1029-1036.

[8] Schnelzer A, Ehlerding A, Blumel C, Okur A, Scheidhauer K, Paepke S and Kiechle M. Showcase of intraoperative 3D imaging of the sentinel lymph node in a breast cancer patient using the new freehand SPECT technology. Breast Care (Basel) 2012; 7: 484-486.

[9] Heuveling DA, Karagozoglu KH, van Schie A, van Weert S, van Lingen A and de Bree R. Sentinel node biopsy using 3D lymphatic mapping by freehand SPECT in early stage oral cancer: a new technique. Clin Otolaryngol 2012; 37: 89-90.

[10] Bluemel C, Schnelzer A, Okur A, Ehlerding A, Paepke S, Scheidhauer K and Kiechle M. Freehand SPECT for image-guided sentinel lymph node biopsy in breast cancer. Eur J Nucl Med Mol Imaging 2013; 40: 1656-1661.

[11] Brouwer OR, Buckle T, Bunschoten A, Kuil J, Vahrmeijer AL, Wendler T, Valdes-Olmos RA, van der Poel HG and van Leeuwen FW. Image navigation as a means to expand the boundaries of fluorescence-guided surgery. Phys Med Biol 2012; 57: 3123-3136.

[12] Valdes Olmos RA, Vidal-Sicart S, Giammarile F, Zaknun JJ, Van Leeuwen FW and Mariani G. The GOSTT concept and hybrid mixed/virtual/augmented reality environment radioguided surgery. Q J Nucl Med Mol Imaging 2014; 58: 207-215.

[13] Brouwer OR, Valdes Olmos RA, Vermeeren L, Hoefnagel CA, Nieweg OE and Horenblas S. SPECT/CT and a portable gamma-camera for image-guided laparoscopic sentinel node biopsy in testicular cancer. J Nucl Med 2011; 52: 551-554.

[14] Brouwer OR, van den Berg NS, Matheron HM, Wendler T, van der Poel HG, Horenblas S, Valdes Olmos RA and van Leeuwen FW. Feasibility of intraoperative navigation to the sentinel node in the groin using preoperatively acquired SPECT/CT data; transferring functional imaging to the operating room. J Urol 2014; 192: 1810-1816.

[15] Ward SR and Lieber RL. Density and hydration of fresh and fixed human skeletal muscle. J Biomech 2005; 38: 2317-2320.

[16] Mariani G, Erba P, Villa G, Gipponi M, Manca G, Boni G, Buffoni F, Castagnola F, Paganelli G and Strauss HW. Lymphoscintigraphic and intraoperative detection of the sentinel lymph node in breast cancer patients: the nuclear medicine perspective. J Surg Oncol 2004; 85: 112-122.

[17] van den Berg NS, Brouwer OR, Klop WM, Karakullukcu B, Zuur CL, Tan IB, Balm AJ, van den Brekel MW, Valdes Olmos RA and van Leeuwen FW. Concomitant radio- and fluorescence-guided sentinel lymph node biopsy in squamous cell carcinoma of the oral cavity using ICG-^{99m}Tc-nanocolloid. Eur J Nucl Med Mol Imaging 2012; 39: 1128-1136.

[18] Bluemel C, Herrmann K, Kubler A, Buck AK, Geissinger E, Wild V, Hartmann S, Lapa C, Linz C and Muller-Richter U. Intraoperative 3-D imaging improves sentinel lymph node biopsy in oral cancer. Eur J Nucl Med Mol Imaging 2014; 41: 2257-64.

[19] Bricou A, Duval MA, Charon Y and Barranger E. Mobile gamma cameras in breast cancer care - a review. Eur J Surg Oncol 2013; 39: 409-416.

[20] Vidal-Sicart S, Rioja ME, Paredes P, Keshtgar MR and Valdes Olmos RA. Contribution of perioperative imaging to radioguided surgery. Q J Nucl Med Mol Imaging 2014; 58: 140-160.

[21] Riccardi L, Gabusi M, Bignotto M, Gregianin M, Vecchiato A and Paiusco M. Assessing good operating conditions for intraoperative imaging of melanoma sentinel nodes by a portable gamma camera. Phys Med 2015; 31: 92-97.

[22] Lombardi A, Nigri G, Scopinaro F, Maggi S, Mattei M, Bonifacino A, Parisella M, Soluri A and Amanti C. High-resolution, handheld camera use for occult breast lesion localization plus sentinel node biopsy (SNOLL): A single-institution experience with 186 patients. Surgeon 2015; 13: 69-72.

[23] Scopinaro F, Tofani A, di Santo G, Di Pietro B, Lombardi A, Lo Russo M, Soluri A, Massari R, Trotta C and Amanti C. High-resolution, handheld camera for sentinel-node detection. Cancer Biother Radiopharm 2008; 23: 43-52.